The Astrophysical Journal, 790:109 (12pp), 2014 August 1 doi:10.1088/0004-637X/790/2/109

FERMI BUBBLES INFLATED BY WINDS LAUNCHED FROM THE HOT ACCRETION FLOW IN SGR A*

Guobin Mou[1,2], Feng Yuan[1], Defu Bu[1], Mouyuan Sun[3,4], and Meng Su[5,6]

[1] Shanghai Astronomical Observatory, Chinese Academy of Sciences, 80 Nandan Road, Shanghai 200030, China; gbmou@shao.ac.cn, fyuan@shao.ac.cn

[2] University of Chinese Academy of Sciences, 19A Yuquan Road, Beijing 100049, China

[3] Department of Astronomy, and Institute of Theoretical Physics and Astrophysics, Xiamen University, Xiamen, Fujian 361005, China

[4] Department of Astronomy and Astrophysics, and Institute for Gravitation and the Cosmos, Pennsylvania State University, University Park, PA 16802, USA

[5] Department of Physics, and Kavli Institute for Astrophysics and Space Research, Massachusetts Institute of Technology, Cambridge, MA 02139, USA

Received 2014 March 9; accepted 2014 June 10; published 2014 July 10

ABSTRACT

A pair of giant gamma-ray Bubbles has been revealed by *Fermi*-LAT. In this paper we investigate their formation mechanism. Observations have indicated that the activity of the supermassive black hole located at the Galactic center, Sgr A*, was much stronger than at the present time. Specifically, one possibility is that while Sgr A* was also in the hot accretion regime, the accretion rate should be 10^3–10^4 times higher during the past $\sim 10^7$ yr. On the other hand, recent magnetohydrodynamic numerical simulations of hot accretion flows have unambiguously shown the existence and obtained the properties of strong winds. Based on this knowledge, by performing three-dimensional hydrodynamical simulations, we show in this paper that the *Fermi* Bubbles could be inflated by winds launched from the "past" hot accretion flow in Sgr A*. In our model, the active phase of Sgr A* is required to last for about 10 million years and it was quenched no more than 0.2 million years ago. The central molecular zone (CMZ) is included and it collimates the wind orientation toward the Galactic poles. Viscosity suppresses the Rayleigh–Taylor and Kelvin–Helmholtz instabilities and results in the smoothness of the Bubbles edge. The main observational features of the Bubbles can be well explained. Specifically, the *ROSAT* X-ray features are interpreted by the shocked interstellar medium and the interaction region between the wind and CMZ gas. The thermal pressure and temperature obtained in our model are consistent with recent *Suzaku* observations.

Key words: accretion, accretion disks – black hole physics – galaxies: active – galaxies: jets – Galaxy: nucleus

Online-only material: color figures

1. INTRODUCTION

Observations have shown that there exists a supermassive black hole (SMBH), Sgr A*, located at the Galactic center (GC). The mass of the black hole is about $4 \times 10^6 M_\odot$ (Schödel et al. 2002; Ghez et al. 2005, 2008; Gillessen et al. 2009a, 2009b). Because of its proximity, Sgr A* is regarded as the best laboratory for studying black hole accretion. Numerous observations have been conducted and abundant data have been obtained (see recent reviews by Genzel et al. 2010; Falcke & Markoff 2013; Yuan & Narayan 2014). The source is currently quite dim, with a bolometric luminosity of only about $10^{36}\,\mathrm{erg\,s^{-1}} \sim 3 \times 10^{-9} L_{\rm Edd}$. The mass accretion rate at the Bondi radius has been estimated by combining *Chandra* observations and the Bondi accretion theory, which is $\sim 10^{-5} M_\odot\ \mathrm{yr^{-1}}$ (Baganoff et al. 2003). The bolometric luminosity would be five orders of magnitude higher if the accretion were in the mode of the standard thin disk. The number of theoretical studies in the past 20 yr have revealed that the advection-dominated accretion flow (ADAF) can explain this puzzle (Yuan et al. 2003). Specifically, the low-luminosity of Sgr A* is because of two reasons. One is the intrinsic low radiative efficiency of ADAF due to energy advection (Narayan & Yi 1994, 1995; Xie & Yuan 2012). Another important reason is the existence of strong wind (or outflow), i.e., ∼99% of the matter captured at the Bondi radius is lost (Yuan et al. 2012a; Narayan et al. 2012; Li et al. 2013). The existence of wind has been confirmed by radio polarization observations (e.g., Aitken et al. 2000; Bower et al. 2003; Marrone et al. 2007), and more recently by the *Chandra* observation of the emission lines from the accretion flow in Sgr A* (Wang et al. 2013). Yuan & Narayan (2014) presented the most recent review on the hot accretion flow and its various astrophysical applications, including Sgr A*.

One particularly interesting thing is that many observational evidences show that the activity of Sgr A* was very likely much stronger in the past than the current stage. These observations suggest that Sgr A* has perhaps undergone multiple past epochs of enhanced activity on different timescales. Here we only focus on relatively long timescales. This evidence was summarized in Totani (2006), and later discussed in other works (e.g., Bland-Hawthorn et al. 2013; Ponti et al. 2013; Kataoka et al. 2013). The evidence includes (1) orders of magnitude higher X-ray luminosity (compared to the present value) required to explain the fluorescent X-ray emission reflected from cold iron atoms in the giant molecular cloud Sgr B2 (Koyama et al. 1996; Murakami et al. 2000, 2001a; Revnivtsev et al. 2004); (2) a new X-ray reflection nebula associated with Sgr C detected by *ASCA* (Murakami et al. 2001b); (3) the ionized halo surrounding Sgr A* (Maeda et al. 2002); (4) the Galactic Center Lobe (GCL; Bland-Hawthorn & Cohen 2003); (5) the Expanding Molecular Ring (EMR; Kaifu et al. 1972; Scoville 1972); (6) the North Polar Spur (NPS; Sofue 2000; Bland-Hawthorn & Cohen 2003); (7) the 8 keV diffuse X-ray emission in the center (Muno et al. 2004); (8) the excess of Hα emission of Magellanic Stream (Bland-Hawthorn et al. 2013); and (9) the *Suzaku* observations of the NPS (Kataoka et al. 2013). Totani (2006) found that to explain the former seven observations mentioned above, the characteristic X-ray luminosity of Sgr A* should be $\sim(10^{39}$–$10^{40})\,\mathrm{erg\,s^{-1}} \sim 2\times(10^{-6}$–$10^{-5})\,L_{\rm Edd}$ several hundred years ago, and such activity should last for $\sim 10^7$ yr. For such a luminosity, the accretion should be well in the regime of hot accretion rather than the standard thin disk

[6] Einstein Fellow.

(Yuan & Narayan 2014). Correspondingly, the mass accretion rate should be 10^3–10^4 times higher than the present value (Totani 2006). Other possibilities for the past activity have also been proposed. For example, the bolometric luminosity in the past millions of years estimated by Bland-Hawthorn et al. (2013) based on the eighth point mentioned above is much higher, $\sim$0.03–0.3 $L_{\rm Edd}$. The timescale of the activity is shorter, and it was active 1–3 Myr ago. Yet another possibility is as follows. A star formation event has been observed and it is believed to have occurred $\sim 6 \times 10^6$ yr ago on scales of $\sim$0.03–0.5 pc from the SMBH (e.g., Genzel et al. 2003; Paumard et al. 2006). If the past activity of Sgr A* occurred concurrently with this event, this would imply that a strong activity of Sgr A* occurred $\sim$6 Myr ago (Zubovas et al. 2011). In summary, so far we still lack a consensus on the past activity of Sgr A*.

Yet perhaps another piece of evidence for the past activity of Sgr A* is the recently detected *Fermi* Bubbles. Using the *Fermi*-LAT, Su et al. (2010) discovered two giant gamma-ray Bubbles located above and below the Galactic plane (also refer to Yang et al. 2014 for recent observations). In Galactic coordinates (l,b), the height of each Bubbles is about 50°, and the width is about 40°. The surface brightness looks uniform, and the edge looks sharp. The total luminosity of the Bubbles is 4×10^{37} erg s^{-1} in 1–100 GeV band. The total energy of the two Bubbles is estimated to be 10^{55}–10^{56} erg.

Many theoretical models have been proposed since the discovery of the *Fermi* Bubbles. In the "hadronic" model, the formation is explained as being due to a population of relic CR protons injected by processes associated with an extremely long timescale and high areal density star formation in the GC (Crocker & Aharonian 2011; Crocker 2012; Crocker et al. 2013). In the "leptonic" scenario the γ-ray emission comes from the inverse Compton scattering between relativistic electrons (also often called cosmic rays) and seed photons. The seed photons may be the cosmic microwave background, but the origin of relativistic electrons is different in different models. They can come from Fermi first-order acceleration on the shock front formed in the periodic star capture processes by Sgr A* (Cheng et al. 2011), the Fermi second-order acceleration through stochastic scattering by plasma instabilities (Mertsch & Sarkar 2011), directly from the jet (Guo & Mathews 2012; Guo et al. 2012; Yang et al. 2012; Yang et al. 2013), or from outflows driven by the past star formation (Carretti et al. 2013).

Among these models, there are two models which are physically most relevant to the model that we propose in the present paper: the "jet" model (Guo & Mathews 2012; Guo et al. 2012) and the "quasar outflow" model (Zubovas et al. 2011; Zubovas & Nayakshin 2012). In the former, it is suggested that the Bubbles are created by an active galactic nucleus (AGN) jet that occurred about 2 Myr ago. After that, cosmic rays (CRs) carried by the jet diffuse to today's morphology. Yang et al. (2012, 2013) developed the jet model by including a magnetic field. They showed that the suppression of the diffusion of CRs along the direction across the edge is caused by the magnetic field configuration. This is because inside the Bubbles the magnetic field is mainly radial, but just outside of the Bubbles and close to the edge, the field is mainly in the parallel direction. One problem, as pointed out by Zubovas et al. (2011), is that they must require the jet direction to be perpendicular to the plane of the Galaxy, which seems to be unlikely, given the general absence of correlation between the direction of jets and galaxy planes and the observed direction of the stellar disk in the Galaxy. In addition, the velocity required in the jet model is as low as $\leqslant 0.1c$ and the mass-loss rate in the jet is in general as high as super-Eddington.

Another model is the "quasar outflow" model proposed in Zubovas et al. (2011) and Zubovas & Nayakshin (2012). In this model, Sgr A* is again assumed to be very active in the past, with mildly super-Eddington accretion rate 6 Myr ago and duration of the activity being 1 Myr. Under such a high-luminosity, quasi-spherical outflow will be driven by the strong radiation pressure from this quasar (King & Pounds 2003), which can result in the formation of the *Fermi* Bubbles. In this model, the existence of the well-known central molecular zone (CMZ) in the GC region plays an important role in collimating the outflow and forming the morphology of the Bubbles. Kataoka et al. (2013) pointed out that the expansion velocity derived by the *Suzaku* observation is lower than the values advocated by both the jet and quasar outflow models by a factor of five and two, respectively.

Assuming that Sgr A* was in an active state as suggested by Totani (2006), in this paper we investigate whether or not the *Fermi* Bubbles can be inflated by the wind launched from the hot accretion flow by performing numerical simulations. In Section 2, we briefly introduce some background on the accretion flow and wind, and present an analytical solution for the interaction between the winds and the interstellar medium (ISM) to be used to understand our numerical simulation results. The numerical simulations approach and the results are presented in Sections 3 and 4, respectively. We then summarize in Section 5.

2. MODELS

2.1. Accretion Flows in Sgr A*

The accretion flow in Sgr A* in the current stage is relatively simple, namely the whole accretion flow is hot, ranging from the Bondi radius to the black hole horizon. However, if the accretion rate is 10^3–10^4 higher, as estimated by Totani (2006), this simple picture needs to be modified. Numerous observational and theoretical studies have shown that the accretion flow should consist of an outer thin disk and an inner hot accretion flow. The boundary between the truncated thin disk and the hot accretion flow is called the transition radius ($R_{\rm tr}$). Some work has been done on the physical mechanism of the transition. Although this question is still not completely solved, we now have a consensus that the value of $R_{\rm tr}$ should decrease with increasing mass accretion rate. This is supported by the modeling of some low-luminosity AGNs and the hard state of black hole X-ray binaries, which is summarized in Yuan & Narayan (2004).

For hot accretion flow, the mass accretion rate is a function of radius because of the mass loss in the wind throughout the disk (refer to Section 2.2). The current net mass accretion rate at the horizon of the black hole and at the Bondi radius are $\sim 10^{-7}\,\dot{M}_{\rm Edd}$ and $10^{-5}\,\dot{M}_{\rm Edd}$, respectively (Yuan et al. 2003). Here $\dot{M}_{\rm Edd} \equiv 10\,L_{\rm Edd}/c^2$ is defined as the Eddington accretion rate. According to Totani (2006), the mass accretion rate close to the horizon of black hole in Sgr A* should be 10^{-4}–$10^{-3}\,\dot{M}_{\rm Edd}$ during the past 10^7 yr. For this value of accretion rate, given the theoretical uncertainty, $R_{\rm tr} = 500R_s$ would be a reasonable assumption; here $R_s = 2GM/c^2$ is the Schwarzschild radius of the black hole. Note that there is some uncertainty in the value of $R_{\rm tr}$. The mass accretion rate at $R_{\rm tr} = 500R_s$ is set to be

$$\dot{M}_{\rm acc}(500R_s) \approx 0.02\,\dot{M}_{\rm Edd} \quad (1)$$

in our favored model. This value is 2×10^3 times higher than the present value, well within the range obtained in Totani (2006).

2.2. Wind

As we have mentioned in Section 1, one characteristic feature of hot accretion flow is that it is subject to strong wind. The existence of wind has been suggested in Narayan & Yi (1994) and later by Blandford & Begelman (1999). The hydrodynamic (HD) and magnetohydrodynamic (MHD) numerical simulation works by Stone et al. (1999) and Stone & Pringle (2001) showed that the mass inflow rate of the accretion flow decreases inward, which can be regarded as the pioneer works in the quantitative study of winds from hot accretion flow. This result is confirmed by many other subsequent works (see review by Yuan et al. 2012b). It was soon shown that the physical reason for the inward decrease of inflow rate is due to mass loss in wind, which occurs in a wide range of radius throughout the accretion flow (Yuan et al. 2012a; Narayan et al. 2012; Li et al. 2013; Sadowski et al. 2013). The physical mechanism for the wind production is found to be the combination of magnetocentrifugal force and the gradient of gas and magnetic pressure (Yuan et al. 2012a; F. Yuan et al. in preparation). While the existence of wind is evident, consensus on some quantitative features of the wind has not been reached. For example, Yuan et al. (2012a) argued that the mass flux of wind should be significant, comparable to the mass flux of inflow. This is much larger than the lower limit obtained in Narayan et al. (2012). In this work, we follow Yuan et al. (2012a) and assume that at $R_{\rm tr}$, the mass flux of wind is roughly equal to the inflow rate there, i.e.,

$$\dot{M}_{\rm wind} \approx 0.02\,\dot{M}_{\rm Edd} \tag{2}$$

in most of our models except for runs "G" and "H" (refer to Table 1).

Yuan et al. (2012a) (see also Li et al. 2013) also estimated the terminal radial velocity of wind based on the conservation of the value of Bernoulli parameter Be and found that it is roughly half of the Keplerian velocity at $R_{\rm tr}$. However, that estimation should be regarded as the lower limit since magnetic field is not included in the analysis. Our more recent study finds that Be actually increases along the streamline when magnetic field is included (F. Yuan et al., in preparation). In the present work we set the velocity of the wind to be

$$v_{\rm wind} \approx 2v_{\rm k}(500R_s). \tag{3}$$

Our simulations indicate that there is some degeneracy between the mass flux and the velocity of the winds. What really matters is the power of the winds. The mass flux and velocity adopted above correspond to the power of wind $P_w = 2\times10^{41}\,{\rm erg\,s^{-1}}$.

The next wind parameter is its angular distribution. In spherical coordinate, F. Yuan et al. (in preparation) find that winds occupy a region $\theta\sim0^\circ$–60° and $\theta\sim120^\circ$–180°. Given that the range is quite large, combined with the possibility that during the long timescale of 10^7 yr the rotation axis of the accretion flow may have changed, in the present work, we simply assume that the winds are blown out isotropically.

Winds may also be launched from the truncated thin disk outside of $R_{\rm tr}$. But the details of this process have been poorly investigated at present. In this work, we assume that this part of wind is not important compared to the winds from the inner hot accretion flow. This is the main uncertainty of our model.

2.3. Shock

The winds launched from the hot accretion flow are usually supersonic so they will interact with the ISM and produce shocks. Before we present the details of our simulation results, in this subsection we present some analytical solutions to this problem based on some simplifications, which is helpful for understanding our simulation results. Here we assume a simple shock model formed by an isotropic wind punching into an isotropic distribution of the ISM. It is well known that the region can be divided into the following four parts: (1) high speed wind, (2) shocked wind, (3) shocked ISM, and (4) un-shocked ISM gas. The interface between the shocked wind and shocked ISM is called the contact discontinuity (CD). In our case, since the cooling timescale of shocked winds is longer than the flow timescale, the shocked wind is an "energy-driven" flow rather than a "momentum-driven" flow (King 2003; Zubovas et al. 2011; Zubovas & King 2012, and Faucher-Giguère & Quataert 2012). If we assume that the forward shock velocity $\dot{R}_2$ is equal to the velocity of the shocked ISM ($v_{\rm c}$) and the shocked ISM region is so thin that $R_c\sim R_2$, we can approximately obtain the following equations (e.g., Castor et al. 1975; Weaver et al. 1977):

$$\dot{E}_b = P_w - 4\pi R_2^2 P_b \dot{R}_2, \tag{4}$$

$$E_b \approx \frac{4}{3}\pi R_2^3\cdot\frac{3}{2}P_b, \tag{5}$$

$$\frac{d}{dt}(M_c\dot{R}_2) = 4\pi R_2^2 P_b, \tag{6}$$

$$M_c = \int_0^{R_2}\rho_{\rm ISM}4\pi r^2 dr, \tag{7}$$

$$P_w = \frac{1}{2}\dot{M}_w V^2. \tag{8}$$

Here, E_b is the total energy of shocked wind, in which the internal energy is dominant, P_w is the kinetic power of the un-shocked wind, P_b is the gas pressure of shocked wind. In the case of weak shock, the shock velocity $\dot{R}_2$ will be significantly higher than the velocity of the shocked ISM, so our approximations may introduce large errors. Assuming $\rho_{\rm ISM} = Ar^{-n}$, in which A and n are both constants and $n<3$, the solutions of the above equations are:

$$R_2(t) = f(A,n)\cdot P_w^{\frac{1}{5-n}}t^{\frac{3}{5-n}}, \tag{9}$$

$$P_b(t) = g(A,n)\cdot P_w^{\frac{2-n}{5-n}}t^{-\frac{n+4}{5-n}}, \tag{10}$$

$$f(A,n) = \left[\frac{(5-n)^3(3-n)}{14\pi A(7-2n)(11-n)}\right]^{\frac{1}{5-n}}, \tag{11}$$

$$g(A,n) = \frac{3A(7-2n)}{(5-n)^2(3-n)}\cdot f(A,n)^{2-n}. \tag{12}$$

Here, R_2 is the radius of the forward shock, and it can roughly be used to represent the radii of CD. Here we have neglected the gravity. This is because in our case the work done by overcoming the gravity is one order of magnitude lower than the injected energy from Sgr A*. Our solution of R_2 is similar to the energy-driven solution in Faucher-Giguère & Quataert (2012). In addition, we find that when the density profile is assumed to be the same as Zubovas et al. (2011), the velocity of the shocked ISM is also close to their result.

Table 1
Parameters of Simulations

Run	n_{e0} (cm^{-3})	R_t (Rs)	v_j[a] (c)	μ ($g\,cm^{-1}\,s^{-1}$)	$\dot{M}_{out}$ ($\dot{M}_{Edd}$)	P_w[b] (10^{41} erg s^{-1})	t_{FB}[c] (Myr)	t_Q[d] (Myr)
A	1.0×10^{-2}	5×10^2	6.2%	2.0	2.0%	2.0	12.3	...
B	1.0×10^{-2}	5×10^2	6.2%	2.0	2.0%	2.0	12.3	0.3
C	1.0×10^{-2}	5×10^2	6.2%	0	2.0%	2.0	7.6	...
D	1.0×10^{-2}	5×10^2	6.2%	4.0	2.0%	2.0	14.5	...
E[e]	1.0×10^{-2}	5×10^2	6.2%	2.0	2.0%	2.0	13.4	...
F	2.0×10^{-2}	5×10^2	6.2%	2.0	2.0%	2.0	14.9	...
G	1.0×10^{-2}	5×10^2	6.2%	3.0	6.0%	6.0	8.1	...
H	1.0×10^{-2}	1×10^3	4.3%	2.0	4.2%	2.0	11.6	...

Notes.
[a] v_j is the velocity of the wind.
[b] P_w is the total kinetic power of the wind injected in 4π of the solid angle.
[c] t_{FB} is the age of the *Fermi* Bubbles.
[d] t_Q is the duration of the quiescent state of Sgr A* in the final stage.
[e] The only difference between E and A is that thermal conductivity is not considered in E.

3. SIMULATION

3.1. Simulation Setup

We use the ZEUS code (Stone & Norman 1992; Hayes et al. 2006) and adopt three-dimensional Cartesian coordinates. The advantage of choosing Cartesian coordinates rather than spherical or cylindrical coordinates is that we can avoid the singularity on the polar axis caused by one term of the viscous stress tensor. Computational domain is from −6.4 kpc to +6.4 kpc in the *X*-,*Y*-direction, and 0–12 kpc in the *Z*-direction. The *Z*-axis stretches along the Galactic pole, and the *X*–*Y* plane is the Galactic plane. Sgr A* is located at the origin. We adopt non-uniform grid, with $\triangle x_{i+1}/\triangle x_i = 1.062$, $\triangle y_{j+1}/\triangle y_j = 1.062$, and $\triangle z_{k+1}/\triangle z_k = 1.035$. The numbers of the meshes are $I = 128$, $J = 128$, and $K = 120$ in the *X*-,*Y*-, and *Z*-directions respectively. We use the reflecting boundary condition on the lower boundary ($Z = 0$), and choose the outflow boundary condition on the other five boundary surfaces.

3.2. Initial Conditions

We assume that the initial ISM is an isothermal sphere in a hydrostatic equilibrium state, i.e., the gradient of the gas pressure balances the gravity. Specifically, we assume the gravitational force given by stars and dark matter in a simplified form:

$$\nabla\phi(r) = -\frac{2\sigma^2}{r}\boldsymbol{r}, \tag{13}$$

where $\boldsymbol{r} = \boldsymbol{x}+\boldsymbol{y}+\boldsymbol{z}$. This will give a constant velocity dispersion of stars, and the velocity dispersion is 100 kms^{-1} here. This is very similar to the circumstance in the galactic bulge. In the recent work by Miller & Bregman (2013), a β-model was assumed to describe the gas density profile of Galactic hole, and n_e scales from 10^{-2}–10^{-1} cm^{-3} at 1 kpc to 10^{-4}–10^{-3} cm^{-3} at 10 kpc. The number density profile of electrons in our simulations is described by the form

$$n_e = \frac{\rho}{\mu_e m_H} = \frac{n_{e0}}{r_{kpc}^{1.6}}, \tag{14}$$

where μ_e^{-1} is the average number of free electrons per nucleon, and $\mu_e \approx 1.17$ for the solar composition, m_H is the atomic mass unit, and n_{e0} is the electron number density at 1 kpc, $r_{kpc} = r/1$ kpc. The value of n_{e0} is 10^{-2} cm^{-3} in the "basic run" (run A), and the density profile in 1–10 kpc is well within the observational range mentioned above, while beyond 10 kpc, the gas has little effect on the *Fermi* Bubbles. More realistic forms of gravity and gas distribution were adopted in Guo & Mathews (2012) and Guo et al. (2012). The simplified form used here would not influence the results significantly, since the difference of density distribution between the two forms is not so large in the bulge or halo. The difference becomes significant close to the Galactic plane, but the *Fermi* Bubbles are far away from the Galactic disk.

The temperature of ISM is 9.2×10^5 K, which is determined by the velocity dispersion σ. The temperature is almost the same as that in Miller & Bregman (2013).

One important massive structure exists in the GC region, i.e., the CMZ (Morris & Serabyn 1996). It is elongated along the Galactic plane, just surrounding Sgr A*, with a total mass of several $10^7 M_\odot$. The length is 400 pc, and the height is 75 pc. As has been shown by Zubovas & Nayakshin (2012), this structure influences the motion of the winds from Sgr A*. It can collimate the winds to the perpendicular direction of the Galactic plane. In the simulation, the CMZ is set to be a torus-like structure located on the *X*–*Y* plane, with inner radius of 80 pc and outer radius of 240 pc. It is in HD equilibrium, and the rotating velocity is $\sqrt{2}\sigma$. The ratio between the height and radius is set to be 0.15 in all runs. From our test simulations, we find that the ratio does not influence the results significantly when it increases from 0.15 to 0.25. The maximum thickness of the CMZ is 72 pc, close to the observational result. The density of the CMZ is set to be a constant. The total mass of the CMZ is set to be $2\times10^7 M_\odot$. As mentioned in Zubovas & Nayakshin (2012), the CMZ cannot be blown away by the winds because the ram pressure force impacting the CMZ is much smaller than the gravitational force. But the top and bottom parts of the CMZ can be affected by the Kelvin–Helmholtz (KH) instability and will form an interesting structure, which can explain X-ray observations (see Section 4.3).

The wind is injected from the inner boundary of the simulation, which has a height of 20 pc and a width of 16 pc. The initial energy density of the ISM around the inner boundary is $\sim2\times10^{-9}$ erg cm^{-3}. This pressure around the black hole supplies a threshold and only winds with ram pressure higher than this value will be able to push the ISM away and induce shocks

in the galactic halo. In most runs of our model, the ram pressure of the wind is about twice the initial pressure of the ISM around the injection region.

3.3. Equations

The HD equations describing the interaction process are as follows. Viscosity and thermal conductivity are included.

$$\frac{d\rho}{dt} + \rho\nabla\cdot\mathbf{v} = 0, \tag{15}$$

$$\rho\frac{d\mathbf{v}}{dt} = -\nabla P - \rho\nabla\Phi + \nabla\cdot\mathbf{T}, \tag{16}$$

$$\frac{\partial e}{\partial t} + \nabla\cdot(e\mathbf{v}) = -P\nabla\cdot\mathbf{v} + \mathbf{T}:\nabla\mathbf{v} + \nabla\cdot(\kappa\nabla T), \tag{17}$$

$$\mathbf{T} = \mu\left(\nabla\mathbf{v} - \frac{2}{3}\mathbf{I}\nabla\cdot\mathbf{v}\right). \tag{18}$$

Here ρ is the density of the gas, P is the gas pressure, e is the internal energy density of the gas, $\mathbf{v}$ is the velocity, $\mathbf{T}$ is the viscous stress tensor, T is temperature, μ is the viscosity coefficient, κ is the heat conductivity coefficient, and $\mathbf{I}$ is the unite tensor. The relationship between the gas pressure and the internal energy density is described by $P = (\gamma - 1)e$. Radiative cooling is neglected. We have estimated the total energy lost by bremsstrahlung cooling within 10 Myr, and found that it is no more than a few percent of the total energy injected by wind.

3.4. Viscosity

The values of viscosity coefficient μ adopted in our models are shown in Table 1. For comparison, we also run a model with $\mu = 0$ (run C). As argued in Guo et al. (2012), the nature of viscosity is still highly uncertain. For a fully ionized, unmagnetized plasma, the dynamical viscosity coefficient is (Spitzer 1962)

$$\mu_{\rm visc} = 6.0\times10^{3}\left(\frac{\ln\Lambda}{37}\right)^{-1}\left(\frac{T}{10^{8}\ {\rm K}}\right)^{5/2}\ {\rm g\,cm^{-1}\,s^{-1}}, \tag{19}$$

where $\ln\Lambda$ is the Coulomb logarithm. The viscosity coefficient is $2\ {\rm g\,cm^{-1}s^{-1}}$ for a typical temperature of 4×10^{6} K in the shocked ISM, and $2\times10^{6}\ {\rm g\,cm^{-1}\,s^{-1}}$ for 10^{8} K inside the Bubbles. In the present work, for simplicity we set the viscosity coefficient to be a constant that is very close to the value in the shocked ISM while quite different from that inside the Bubbles. But in the CMZ region we calculate the viscosity coefficient according to Equation (19). CMZ gas will not suffer from the effect of viscosity since the viscosity coefficient is very low there.

As pointed out by Guo et al. (2012), viscosity plays an important role because it can suppress instabilities so that we can obtain a smooth edge of the Bubbles. The value of viscosity also influences the width of the Bubbles. We will discuss this point in more detail in Section 4.4.

3.5. Thermal Conductivity

We also include thermal conduction in all of our models except for run E. This makes the distribution of gas inside the Bubbles uniform. The heat flux Q is given by

$$Q = -\kappa\nabla T; \tag{20}$$

here κ is the coefficient of thermal conductivity. For a fully ionized gas, κ is given by (Spitzer 1962)

$$\kappa \approx 2\times10^{-4}\frac{T^{5/2}}{Z^{4}\ln\Lambda}\ {\rm erg\,s^{-1}\,K^{-1}\,cm^{-1}}. \tag{21}$$

In reality, thermal conduction will be strongly affected by the magnetic field. Specifically, in the direction perpendicular to the magnetic field, thermal conduction will be strongly suppressed because it is difficult for the particles to move across the field lines. In addition, in a collisionless fluid, thermal conduction would be saturated, but the calculation of heat flux in this case is still on a phenomenological level with an artificially assumed factor (Cowie & McKee 1977). We find that our results are not sensitive to the value of κ. Even a value of the coefficient of thermal conductivity orders of magnitude lower than that determined by Equation (21) is enough to smooth the distribution of gas within the Bubbles.

4. RESULTS

4.1. Morphology

In our model, we identify the CD to be the edge of the observed *Fermi* Bubbles. The region of shocked ISM is the "surrounding region." When the magnetic field is included, the field lines in this region will be aligned with the CD, which prevents the diffusion of relativistic electrons across the Bubbles' edge. This then explains why the edge of the Bubbles is so sharp (Yang et al. 2012). This mechanism also applies to our model since in reality the magnetic field should exist.

If we only want to explain the morphology of the Bubbles, we find that we have relatively large freedom in terms of the values of velocity and mass flux of the winds. For example, we can use a smaller wind velocity and a higher mass outflow rate, or a larger wind velocity and a lower mass outflow rate to get the "correct" morphology. However, observations add additional constraints, such as temperature. We choose run A as our "basic run" because not only the morphology but also other properties of the Bubbles are consistent with observations. In run A, winds need to last for 12.3 Myr to get the "correct" morphology of the Bubbles, as shown by Figure 1. The height and width of the Bubbles are 8 kpc and 7 kpc, respectively, which corresponds to a projected Bubble with a latitude of 50° and a longitude of 50°. Although the wind is set to be injected isotropically, the massive CMZ surrounding Sgr A* blocks the lateral movement of the winds, and forces them to move upward. In other words, the CMZ successfully collimates the winds to the perpendicular direction of the Galactic plane. This is why we can obtain a Bubble with a narrow waist near the Galactic plane, instead of a hemispherical Bubble buckling on the Galactic plane.

We have tried to explore when the activity of Sgr A* quenched and entered into a quiescent state by running "run B." We find that only if the quiescent time is shorter than 0.2 Myr, will the result not be affected, i.e., showing a significant conical structure in the X-ray band with latitude $|b| \lesssim 10°$ (see lower panels in Figure 3). Because the quiescent timescale is so short compared with the age of the *Fermi* Bubbles, even though in all other runs in this work Sgr A* does not enter into the quiescent state as it should be, our simulation results will not be affected.

4.2. Energy, Mass, and Temperature

For run A, the total energy injected by Sgr A* is about 7.7×10^{55} erg. This energy is comparable to the injected energy

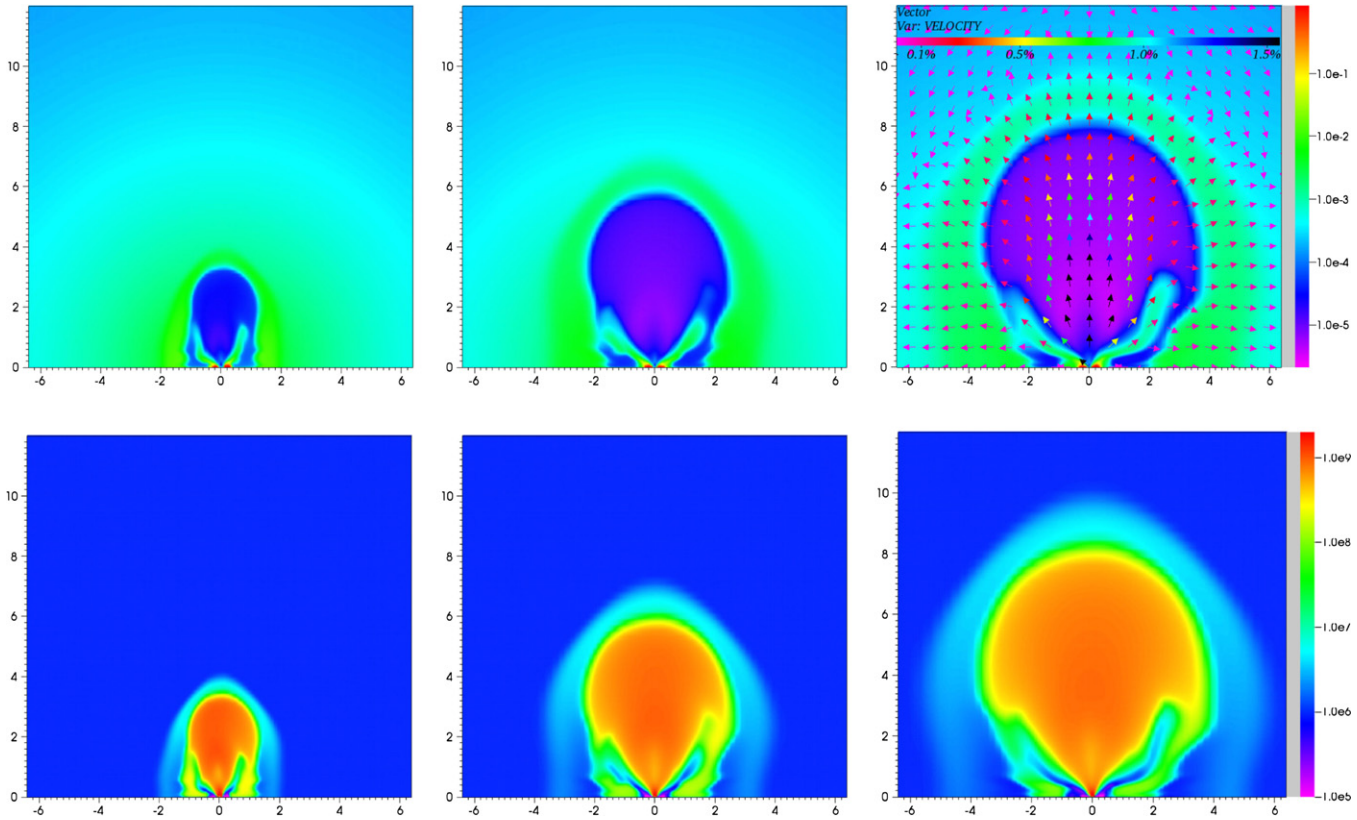

Figure 1. Evolution of morphology in run A (X–Z slice) for the number density (top panel) and temperature (bottom panel). From left to right, the plots correspond to $t = 4$, 8, and 12.3 Myr, respectively. The velocity field is added in the top right panel with values in units of the light speed.

(A color version of this figure is available in the online journal.)

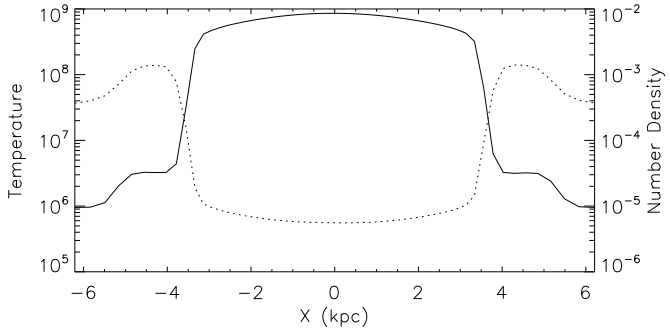

Figure 2. Profiles of temperature (solid line) and electron number density (dotted line) along the X-axis for run A at $t = 12.3$ Myr, averaged from $z = 4.5$ kpc to 6.0 kpc. Temperature is in kelvin, while number density is in units of cm^{-3}. From this figure, we can see that the average temperature inside the Bubbles is $\sim 6 \times 10^8$ K, while in the surrounding region it is $\sim 3 \times 10^6$ K.

from GC estimated from some observations to some structures, such as the NPS structure, GCL, and EMR (Totani 2006). The total internal energy of the *Fermi* Bubbles in our simulation is 2.2×10^{55} erg, which is consistent with the observational value. The total kinetic energy of the *Fermi* Bubbles is only 2×10^{54} erg, much smaller than the internal energy. This is because the speed of the gas inside the Bubbles is subsonic.

The total mass inside the Bubbles is about a few times $10^5 M_\odot$, which is much lower than the estimation of $10^8 M_\odot$ based on the assumed upper limit of an average density $n \sim 10^{-2}$ cm^{-3} in Su et al. (2010). This is because the density in our simulation is about three orders of magnitudes lower than the assumed value in Su et al. (2010), as shown by Figure 2. We add the following comments to this "discrepancy." First, our observational constraint on the density is poor, and thus the total mass of $10^8 M_\odot$ is subject to a large uncertainty. Second, since the coefficient of thermal conductivity adopted in our work is low, we may have underestimated the evaporation process, which may play an important role in transporting mass from the surrounding gas, including CMZ and shocked ISM, into the Bubbles. Third, we assume the ISM to be homogeneous for simplicity, while in reality the ISM is likely to be clumpy. The dense clouds may be difficult to be blown away by the winds so they will stay inside the Bubbles, which will significantly increase the mass of the gas within the Bubbles.

The temperature of the gas is determined by the following equation:

$$T = \frac{(\gamma - 1) e \mu m_H}{k \rho}, \tag{22}$$

where T is temperature, μ is the molecular weight, which is 0.61 for solar composition. Temperatures of different runs are given in Table 2. In general, the temperature inside the Bubbles is several times 10^8 K. Although there are some new results of Milky Way's hot halo recently, the temperature inside the *Fermi* Bubbles is still lacking data. So our result can be regarded as a prediction. We will discuss the temperature in the surrounding region between the CD and the forward shock in Section 4.3.

4.3. X-Ray Structure

We have calculated the predicted X-ray image by considering the bremsstrahlung radiation. Figure 3 shows the result. We can see that the morphology is consistent with the limb-brightened X-ray structure obtained in *ROSAT* observations (Snowden et al.

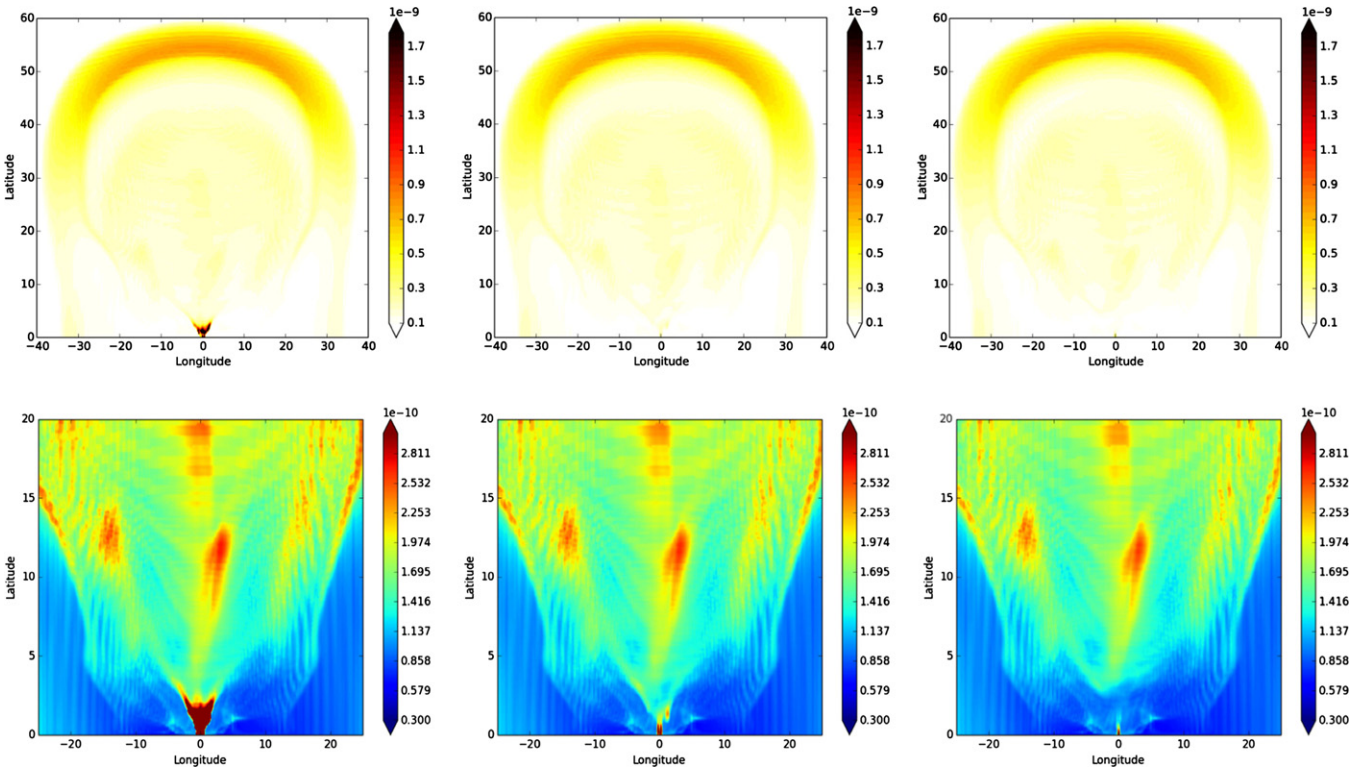

Figure 3. X-ray structure in R6+R7 band (0.5 keV–1.5 keV) obtained from run B. Top and bottom panels are for different spacial scales, with the bottom one zooming in the center part near the Galactic center (GC). For each panel, from left to right, the plots correspond to different time durations (δt) from the quenching of the Sgr A* activity, with $\delta t = 0.1$, 0.2, and 0.3 Myr, respectively. The brightness of the inner conical structure gradually dims out. For the bottom left plot, both the limb-brightened surrounding structure outside the Bubbles and the conical structure near the GC are clearly seen, in good consistency with observations (Snowden et al. 1997; Wang 2002). For the middle one, this structure is significantly weaker, while for the right one the structure in $|b| \lesssim 5^\circ$ begins to disappear.

(A color version of this figure is available in the online journal.)

Table 2
Results

Run	H/W[a]	T_{FB}[b] (10^8 K)	T_X[c] (10^6 K)	E_{FB}[d] (10^{55}erg)	K_{FB}[e] (10^{55}erg)	E_X[f] (10^{55}erg)	K_X[g] (10^{55}erg)	E_{inj}[h] (10^{55}erg)	M_{inj}[i] ($M_\odot$)	M_{FB}[j] ($M_\odot$)
A	8/7	5	3	2.2	0.2	3.5	2.1	7.7	2×10^4	2.5×10^5
B	8/7	5	3	2.2	0.1	3.6	2.1	7.6	2×10^4	2.5×10^5
C	10/4	3	3	0.7	0.4	1.9	0.9	4.7	1×10^4	1.2×10^5
D	8/8.5	5	3	2.7	0.2	4.4	2.8	9.2	3×10^4	2.9×10^5
E	8/8	10	3	2.5	0.2	3.9	2.5	8.4	2×10^4	3.0×10^5
F	8/7	5	3	2.7	0.2	5.2	2.4	9.4	3×10^4	3.5×10^5
G	8/6.5	7	5	4.5	0.7	5.7	4.6	15.2	4×10^4	4.5×10^5
H	8/7	4	3	2.0	0.3	3.3	2.0	7.2	4×10^4	2.8×10^5

Notes. [a] Height/width of the *Fermi* bubbles, in units of kpc/kpc. [b] T_{FB} is the space-averaged temperature of *Fermi* Bubbles. [c] T_X is the space-averaged temperature of shocked ISM. [d] E_{FB} is the internal energy of *Fermi* Bubbles. [e] K_{FB} is the kinetic energy of *Fermi* Bubbles. [f] E_X is the internal energy of shocked ISM. [g] K_X is the kinetic energy of shocked ISM. [h] E_{tot} is the total energy injected by Sgr A* wind. [i] M_{inj} is the total mass injected from the origin. [j] M_{FB} is the total mass of the *Fermi* Bubbles.

1997; Su et al. 2010). This structure corresponds to the shocked ISM. Here, we only calculate the bremsstrahlung radiation, so our images are only for qualitative comparison. The temperature inside the Bubbles is two orders of magnitude higher than the surrounding region while the density is two orders of magnitude lower. Therefore the outer region is much brighter than the interior of the Bubbles in the X-ray band.

Recent *Suzaku* observations have revealed that the temperature of the surrounding region at high latitude ($\gtrsim +40^\circ$) is around 0.3 keV and the thermal pressure is 2×10^{-12} dyn cm^{-2} (Kataoka et al. 2013). Our model is consistent with their results. In run A, the temperature and thermal pressure in the same location are 0.4 keV and 1.2×10^{-12} dyn cm^{-2}, respectively (also see Table 2, note that the temperature is space-averaged value of the shocked ISM). In contrast, in the jet model and the quasar outflow model, the predicted temperature is larger than a few keV (Guo & Mathews 2012; Yang et al. 2012; Barkov & Bosch-Ramon 2014) and 1 keV (Zubovas & Nayakshin 2012), respectively. We think that the main reason for such a discrepancy is that the wind velocities, and more importantly the mass fluxes of the winds, in these two models are too high.

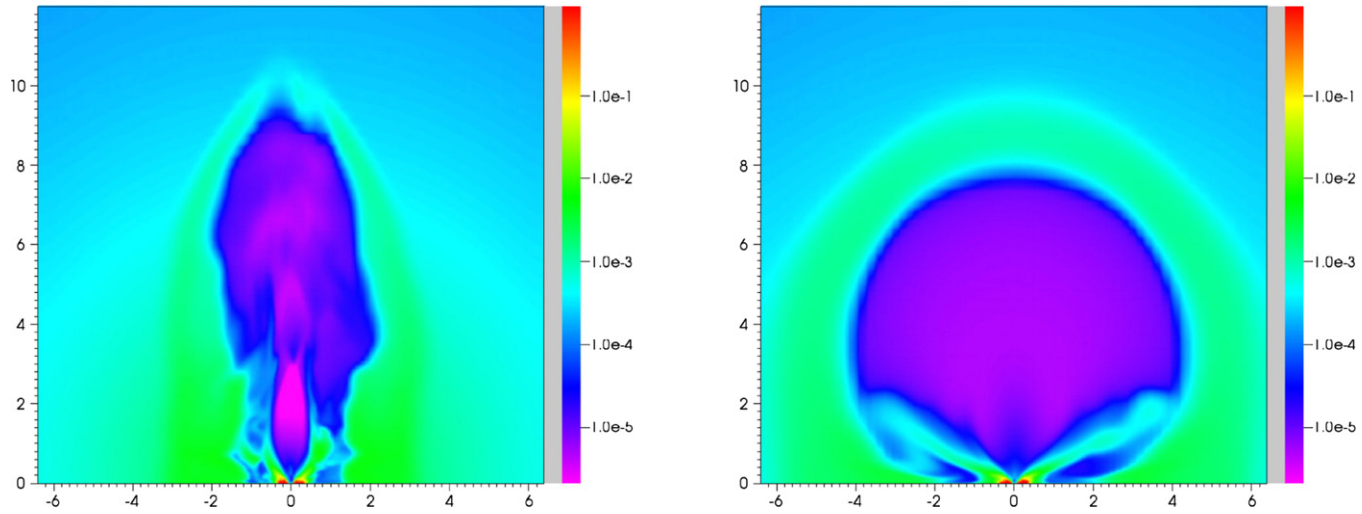

Figure 4. Effect of the viscosity coefficient on the morphology of the Bubble. The left and right plots show the number density of electrons for run C (without viscosity) at $t = 7.6$ Myr and run D (with large viscosity) at $t = 14.5$ Myr, respectively (X−Z slice). When the viscosity coefficient is higher, the Bubble becomes more spherical.

(A color version of this figure is available in the online journal.)

We have calculated the bremsstrahlung radiation, and found that the total lost energy is no more than 10 percent of the total internal energy of the surrounding region, so the cooling effect is very weak. We note that the interaction region between the winds and the CMZ gas is also quite bright in the X-ray band, which looks like a cone upside-down on the Galactic plane. This structure explains the features observed in the *ROSAT* X-ray survey by Snowden et al. (1997) and Wang (2002).

As we have mentioned in Section 4.1, the brightness of the conical X-ray structure near the GC observed in 0.5–1.5 keV is related to the time duration starting from the quenching of the past activity of Sgr A*. From run B, we find that the time duration should be no more than ∼0.2 Myr. Observations also show that we can only see the east (left) X-ray structure of the northern sky. Together with the bending of the northern *Fermi* Bubbles, we speculate that this phenomenon may be caused by the galactic wind blowing from the east to the west in the northern sky. Hence, the forward shock in the east will be stronger than in the west, and both the temperature and the density of the shocked ISM in the east will be larger than in the west, inducing the asymmetric structure of X-ray emission. Another possibility is that the initial ISM is not symmetric, with the density in the left (east) part being higher.

The *ROSAT* X-ray structure looks like an X-ray cavity. Such kinds of cavities have also been observed in other galaxies or galaxy clusters. Usually people think that they are formed by the interaction between jets and the ISM or intergalactic medium (IGM). However, our result reminds us that these cavities may be well formed by the interaction between the winds (rather than jet!) from the central AGN and the IGM. As pointed out by Young et al. (2002) and Di Matteo et al. (2003) in the case of the cavity in M87, if the cavity were formed by the jet, we would expect sharp bow shock regions between a jet and the surrounding medium. This structure has never been observed.

4.4. The Effects of Viscosity and Thermal Conduction

The morphology also depends on the viscosity coefficient μ, as shown by Figure 4. We can see from the figure that if the viscosity coefficient is larger, the Bubbles will be more spherical. The winds near the CMZ suffer from the viscous force because of the large velocity gradient on the $X-Y$ plane, and they are slowed down by the CMZ significantly. If the viscosity coefficient is larger, the kinetic energy of wind gas will be dissipated into internal energy more efficiently, then the thermal pressure close to the GC will be larger. Therefore, the opening angle of the blown-up CMZ gas will be wider, which causes the Bubbles to be more spherical.

Viscosity can suppress both the Rayleigh–Taylor (RT) and KH instabilities. Following Equations (18) and (19) from Yang et al. (2012), we can estimate the timescales for the growth of both instabilities. For example, for the RT instability to form a ∼1 kpc structure at a height of $z = 4$ kpc, the required timescale is about 5 Myr, while for the KH instability it is about 1.5 Myr. So both instabilities can grow during the formation of the *Fermi* Bubbles. From the left plot of Figure 4 we can see that, when viscosity is not included, large rolls with typical length scales of ∼ kpc inside the shocked ISM are formed. However, for all the other runs with viscosity included, no such rolls are found.

Another role of viscosity is viscous heating. This effect is important in the interaction region between winds and CMZ. In this region, the main components of viscous stress tensor are T_{xz} $(= T_{zx})$ and T_{yz} $(= T_{zy})$,

$$\frac{\partial e}{\partial t} \sim T_{xz}\frac{\partial v_x}{\partial z} + T_{yz}\frac{\partial v_y}{\partial z}. \quad (23)$$

For the interaction region, $T_{xz} \simeq \mu \partial v_x/\partial z$. Replacing ∂v_x with $0.1\%c$ and ∂z with 100 pc, we can estimate that the timescale for the winds to pass through this region is ∼1 Myr. The density of the CMZ gas blown up in the interaction region is $\sim 10^{-2}\mathrm{cm}^{-3}$. Then the increase of temperature is $\sim 10^6$ K.

What is the role of thermal conduction? We study this problem in run E (without thermal conduction). Figure 5 shows the distribution of the electron number density and temperature. A jet-like structure along the z-axis is clearly seen. Since the grids along the z-axis are elongated, we need to check whether or not this feature is artificial. We have done such a test and found that this feature is likely real. The temperature of this structure is relatively low, but the density is high. Their formation

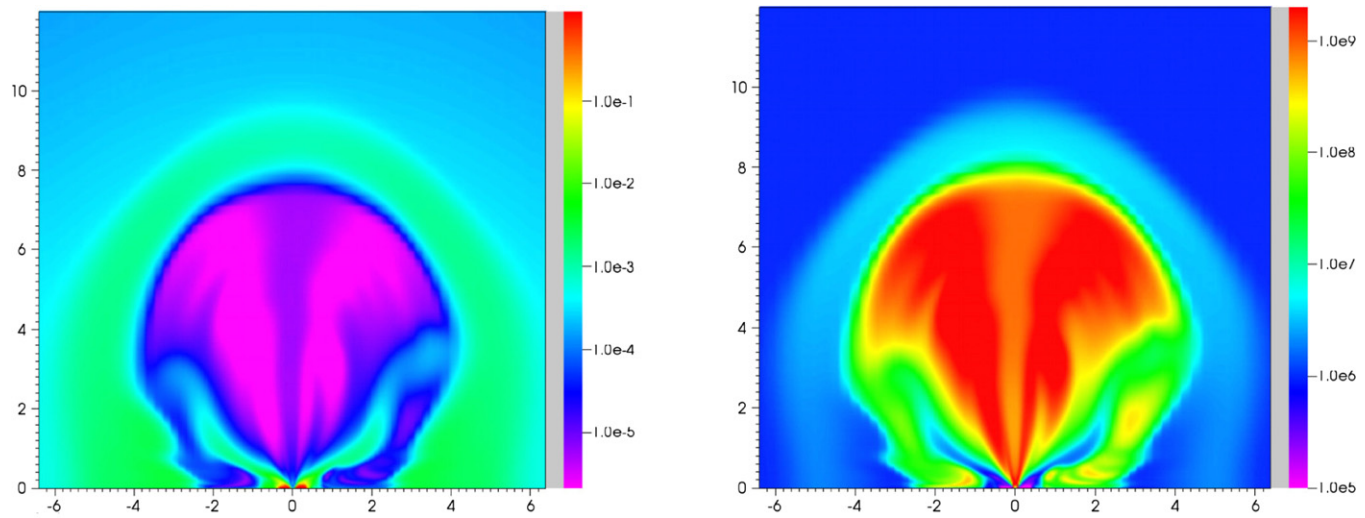

Figure 5. Distributions of electron number density (left) and temperature (right) at the $Y = 0$ plane for run E (without thermal conduction) at $t = 13.4$ Myr. Compared with Figure 1, we can see that there is a "jet-like" feature with lower temperature and higher density through the middle of the Bubbles. This feature disappears when thermal conduction is included.

(A color version of this figure is available in the online journal.)

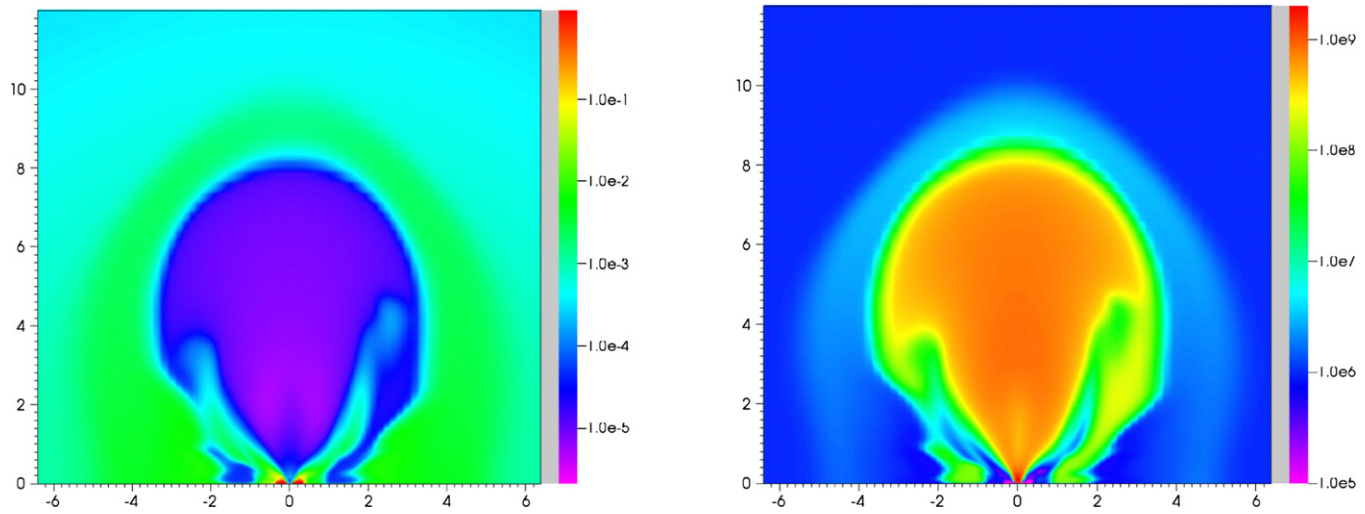

Figure 6. Distributions of density (left) and temperature (right) on the $Y = 0$ plane for run F at $t = 14.9$ Myr. In this model, the density of the ISM is two times higher than run A. In this case, more time is needed to form the Bubbles. Both the density and the temperature inside the Bubbles are higher while the temperature of the surrounding structure is lower because of the lower speed of the forward shock.

(A color version of this figure is available in the online journal.)

mechanism is as follows. In the inner region, the massive CMZ gas acts like a wall around Sgr A*, preventing the winds from expanding in the horizontal direction. The winds collide with the CMZ and the kinetic energy of winds is converted into thermal energy, and thus the temperature and pressure increase. The high-pressure gas then escapes toward the polar direction, squeezing the wind from Sgr A* and causing the formation of this jet-like structure. However, when we include thermal conduction as in most of our runs, this structure disappears. This is because thermal conduction can efficiently transport energy between the regions with different temperatures, thus smoothing out this structure.

4.5. The Role of ISM Density

For simplification, we have adopted a power-law distribution for the density distribution of the initial ISM: $\rho = A/r^n$, where A and n are constants, and r is in units of 20 pc in our simulations. The value of A has a weak influence on the age of the *Fermi* Bubbles. This can be seen in run F (refer to Figure 6). Although the density is two times higher than the basic run, it only takes 20% more time to form the Bubbles. This is easy to understand from Equations (9) and (11).

Different from the parameter A, the value of n is more important for influencing the evolution of the Bubbles. For example, our simulations show that if the index n is changed into 2.0 from 1.6 while A remains unchanged compared to run F, then the age of the Bubbles would be 7 Myr, which is half the age of run F. The temperature of the shocked ISM at a latitude of $\gtrsim +40^\circ$ is about 1 keV in this case. Physically, this is because the kinetic energy of the shocked ISM is nearly a constant fraction of the total energy injected from the GC. Specifically, from Equations (9) and (11), we can obtain

$$\frac{1}{2} M_c \dot{R}_2^2 = 2\pi A \frac{f^{5-n}}{3-n} P_w t, \tag{24}$$

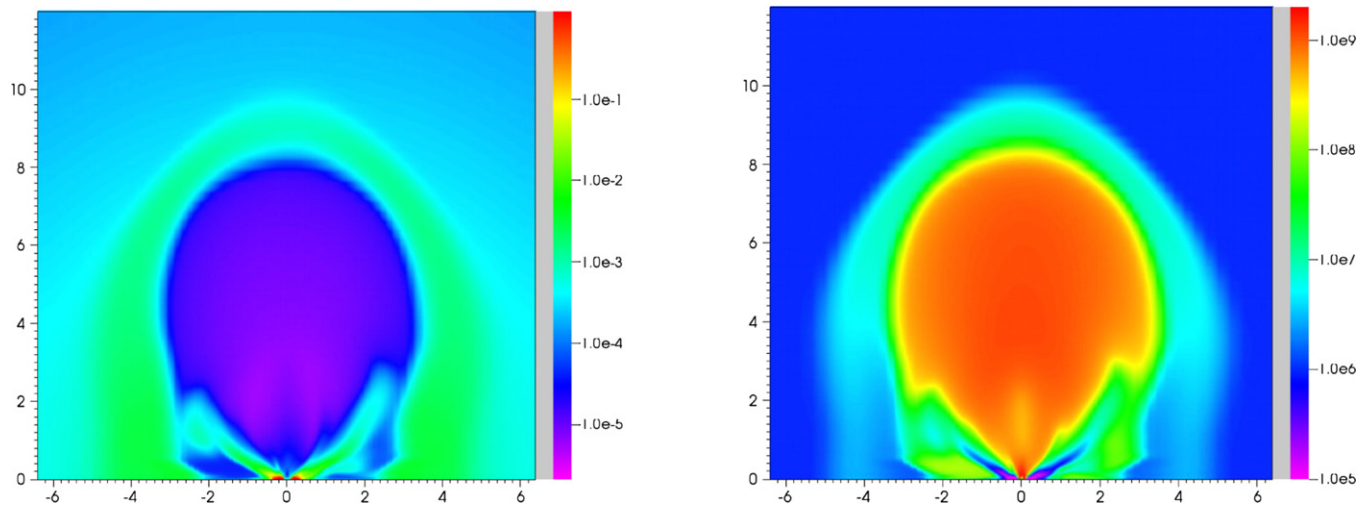

Figure 7. Distributions of number density (left) and temperature (right) of electrons on the $Y = 0$ plane for run G (with a higher mass outflow rate than run A) at $t = 8.1$ Myr. Compared with Figure 1, we can see that the density inside the Bubbles is larger, and the temperature in the whole region is higher.

(A color version of this figure is available in the online journal.)

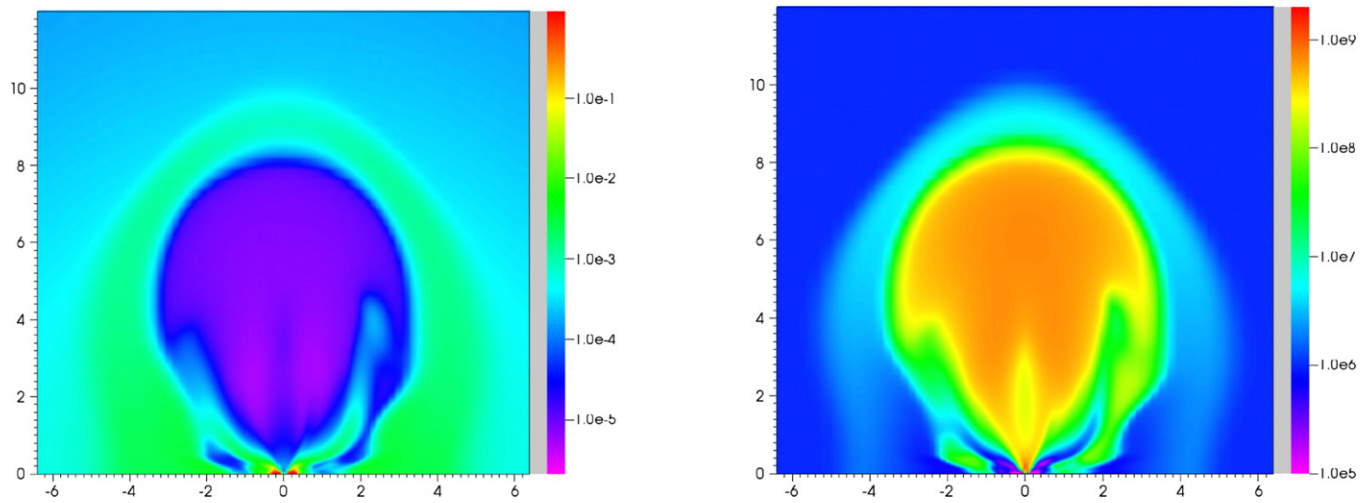

Figure 8. Distributions of number density (left) and temperature (right) of electrons on the $Y = 0$ plane for run H (with a larger transition radius $R_{\rm tr}$ than run A) at $t = 11.6$ Myr.

(A color version of this figure is available in the online journal.)

where M_c and $\dot{R}_2$ are the mass and velocity of shocked ISM, respectively. We find that $2\pi A(f^{5-n}/(3-n))$ is almost a constant: ~0.3. Therefore, we can approximately rewrite the right-hand side of Equation (24) as $\eta P_w t = (1/2) M_c \dot{R}_2^2 \sim (1/2) M_c R_2^2/t^2$ (η is a constant), or $t \propto M_c^{1/3}$ when P_w remains unchanged. For the two cases mentioned above, if A is doubled, M_c is doubled, while n changed from 1.6 to 2.0, and M_c is only one-eighth of the former. That is why the ages are 20% larger and one-half smaller, respectively.

4.6. The Role of the Wind Parameters

In run G (see Figure 7), the mass flux of the winds is three times higher than run A, while the wind velocity is the same. The age is 34% shorter than run A. This is very close to the result of 31% by the simple analytical analysis shown by Equation (9). Because of the increase of the wind power, the velocity of the forward shock increases, and thus the temperature of the shocked ISM becomes higher, while the increase of temperature inside the Bubbles is not so obvious.

In run H (see Figure 8), we reduce the wind velocity but keep the kinetic power of wind (P_w) unchanged compared to run A. We find that the kinetic and thermal energy and temperature of different regions do not change much (refer to Table 2). This means that the results mainly depend on the kinetic power, while the velocity and mass outflow rate are degenerate. This is also easy to understand from Equations (9) and (10).

The gas inside the Bubbles mainly comes from the blown-up CMZ gas instead of winds injected from Sgr A*. In addition, the evaporation of the Bubbles' edge, which is determined by thermal conduction, should also supply additional gas. But since there is large uncertainty in the thermal conduction coefficient, it is hard for our model to predict the exact mass of the gas inside the Bubbles. In addition to the total mass, another interesting quantity is the temperature of the gas inside the Bubbles. To estimate the temperature, we need to know the pressure. This quantity is equal to the gas pressure of the shocked ISM, which

is well determined by the density of the ISM and the wind power from Equation (10). Unfortunately, the uncertainty of the gas density inside the Bubbles mentioned above makes it hard to precisely predict the temperature. Based on our simulation of run A, we can only estimate the temperature of gas within the Bubbles to be in the range of $10^8 \sim 10^9$ K. Observational constraints are still lacking.

5. SUMMARY AND DISCUSSION

We have performed hydrodynamical numerical simulations to study the formation mechanism of the *Fermi* Bubbles detected by *Fermi*-LAT. Our main aim in the present paper is to explain the morphology and the thermodynamical properties of the Bubbles, but we leave the study of the production of γ-ray photons and the explanation of the spectrum for our next work. While Sgr A* is quite dim at the present stage, many observational evidences indicate that this source should be much more active in the past. Specifically, one possibility suggested by a previous work is that the mass accretion rate of the hot accretion flow in Sgr A* should be 10^3–10^4 times higher than the present value and this activity lasts for several Myr (Totani 2006). Based on this scenario, we show that the observed *Fermi* Bubbles can be well formed by the interaction between the winds launched from the "past" hot accretion flow and ISM. In our model, the winds last for 10^7 yr and the activity of Sgr A* was quenched no more than 0.2 Myr ago. The properties of wind such as the mass flux and velocity are not free parameters but are obtained from previous works on MHD numerical simulations of hot accretion flows. Viscosity and thermal conduction are included, which can suppress various instabilities and make the gas inside the Bubbles uniform. The required power of the winds is $\sim 2 \times 10^{41}$ erg s^{-1}, which is fully consistent with previous studies on the past activity of Sgr A*. The edge of the Bubbles corresponds to the CD, which is the boundary between the shocked ISM and the shocked winds. Properties of the Bubbles such as the morphology and the total energy are consistent with observations. The limb-brightened *ROSAT* X-ray structure can be interpreted by the shocked ISM behind the forward shock, while the conical-like X-ray structure close to the GC is interpreted by the interaction region of wind gas and CMZ gas. Our model can also quantitatively explain both the thermal pressure and the temperature of the X-ray structure at high latitude ($\gtrsim +40^\circ$) revealed by recent *Suzaku* observations.

In addition to winds, jets should also coexist with hot accretion flow (Yuan & Narayan 2014). In our model, we do not include the jet. We assume that the interaction between the jet and the ISM is negligible because, by definition, the jet must be well collimated and be as fast as the light. In this case, we expect that the jet will simply drill through the ISM, with almost no interaction with the ISM in the Galaxy.

We have also calculated the energy transformation efficiency in our model. We find that at $r \sim 10$ kpc, $\sim$60% of the total energy of winds injected from Sgr A* is transported into the ISM. Obviously, such a high efficiency is due to the large opening angle of winds. This result suggests that we may consider the role of winds in solving the cooling flow problem in some elliptical galaxies and galaxy clusters. Usually people consider the heating of ISM or intracluster medium by jets (see, e.g., Vernaleo & Reynolds 2006 and references therein). However, numerical simulations have found that jet may only be able to deposit their energy at $r > 100$ kpc, and thus not be very efficient (Vernaleo & Reynolds 2006). Some solutions have been suggested, e.g., the precession of a jet, or the motions of an intracluster medium (see Vernaleo & Reynolds 2006 and Heinz et al. 2006). But another possible way is to invoke winds whose existence has been firmly established by both observational and theoretical studies. Given our successful explanation of the formation of the *Fermi* Bubbles using the wind model, it would also be worthwhile to study whether or not the X-ray cavities observed in galaxy clusters (e.g., Fabian 2013), which have a similar morphology to the *Fermi* Bubbles, can be produced by winds.

We thank Fuguo Xie, Zhaoming Gan, Tomohisa Kawashima, Chao Liu, Hui Li, and Daniel Wang for helpful discussions. We also thank the referee for constructive suggestions. This work was supported in part by the Natural Science Foundation of China (grants 11103061, 11133005, 11121062, and 11103059), the National Basic Research Program of China (973 Program, grant 2014CB845800), and the Strategic Priority Research Program "The Emergence of Cosmological Structures" of the Chinese Academy of Sciences (grant XDB09000000). M.Y.S. acknowledges support from the China Scholarship Council (No. [2013]3009). Support for the work of M.S. was provided by NASA through Einstein Postdoctoral Fellowship grant number PF2-130102 awarded by the Chandra X-ray Center, which is operated by the Smithsonian Astrophysical Observatory for NASA under contract NAS8-03060. The simulations were carried out at SHAO Super Computing Platform.

REFERENCES

Aitken, D. K., Greaves, J., Chrysostomou, A., et al. 2000, ApJL, 534, L173
Baganoff, F. K., Maeda, Y., Morris, M., et al. 2003, ApJ, 591, 891
Barkov, M. V., & Bosch-Ramon, V. 2014, A&A, 565, 65
Blandford, R. D., & Begelman, M. C. 1999, MNRAS, 303, L1
Bland-Hawthorn, J., & Cohen, M. 2003, ApJ, 582, 246
Bland-Hawthorn, J., Maloney, P. R., Sutherland, R. S., & Madsen, G. J. 2013, ApJ, 778, 58
Bower, G. C., Wright, M. C. H., Falcke, H., & Backer, D. C. 2003, ApJ, 588, 331
Carretti, E., Crocker, R. M., Staveley-Smith, L., et al. 2013, Natur, 493, 66
Castor, J., McCray, R., & Weaver, R. 1975, ApJL, 200, L107
Cheng, K.-S., Chernyshov, D. O., Dogiel, V. A., et al. 2011, ApJL, 731, L17
Cowie, L. L., & McKee, C. F. 1977, ApJ, 211, 135
Crocker, R. M. 2012, MNRAS, 423, 3512
Crocker, R. M., & Aharonian, F. 2011, PhRvL, 106, 101102
Crocker, R. M., Bicknell, G. V., Carretti, E., et al. 2013, arXiv:1312.0692
Di Matteo, T., Allen, S. W., Fabian, A. C., et al. 2003, ApJ, 582, 133
Fabian, A. C. 2012, ARA&A, 50, 455
Falcke, H., & Markoff, S. 2013, CQGra, 30, 244003
Faucher-Giguère, C., & Quataert, E. 2012, MNRAS, 425, 605
Genzel, R., Eisenhauer, F., & Gillessen, S. 2010, RvMP, 82, 3121
Genzel, R., Schödel, R., Ott, T., et al. 2003, ApJ, 594, 812
Ghez, A. M., Salim, S., Hornstein, S. D., et al. 2005, ApJ, 620, 744
Ghez, A. M., Salim, S., Weinberg, N. N., et al. 2008, ApJ, 689, 1044
Gillessen, S., Eisenhauer, F., Fritz, T. K., et al. 2009a, ApJL, 707, L114
Gillessen, S., Eisenhauer, F., Trippe, S., et al. 2009b, ApJ, 692, 1075
Guo, F., & Mathews, W. G. 2012, ApJ, 756, 181
Guo, F., Mathews, W. G., Dobler, G., & Oh, S. P. 2012, ApJ, 756, 182
Hayes, J. C., Norman, M. L., Fiedler, R. A., et al. 2006, ApJS, 165, 188
Heinz, M., Brüggen, M., Young, A., & Levesque, E. 2006, MNRAS, 373, L65
Kaifu, N., Kato, T., & Iguchi, T. 1972, Natur, 238, 105
Kataoka, J., Tahara, M., Totani, T., et al. 2013, ApJ, 779, 57
King, A. R. 2003, ApJL, 596, L27
King, A. R., & Pounds, K. A. 2003, MNRAS, 345, 657
Koyama, K., Maeda, Y., Sonobe, T., et al. 1996, PASJ, 48, 249
Li, J., Ostriker, J., & Sunyaev, R. 2013, ApJ, 767, 105
Maeda, Y., Baganoff, F. K., Feigelson, E. D., et al. 2002, ApJ, 570, 671
Marrone, D. P., Moran, J. M., Zhao, J. H., & Rao, R. 2007, ApJL, 654, L57
Mertsch, P., & Sarkar, S. 2011, PhRvL, 107, 091101
Miller, M. J., & Bregman, J. N. 2013, ApJ, 770, 118
Morris, M., & Serabyn, E. 1996, ARA&A, 34, 645

Muno, M. P., Baganoff, F. K., Bautz, M. W., et al. 2004, ApJ, 613, 326
Murakami, H., Koyama, K., & Maeda, Y. 2001a, ApJ, 558, 687
Murakami, H., Koyama, K., Sakano, M., et al. 2000, ApJ, 534, 283
Murakami, H., Koyama, K., Tsujimoto, M., et al. 2001b, ApJ, 550, 297
Narayan, R., Sadowski, A., Penna, R. F., & Kulkarni, A. K. 2012, MNRAS, 426, 3241
Narayan, R., & Yi, I. 1994, ApJL, 428, L13
Narayan, R., & Yi, I. 1995, ApJ, 452, 710
Paumard, T., Genzel, R., Martins, F., et al. 2006, ApJ, 643, 1011
Ponti, G., Morris, M. R., Terrier, R., & Goldwurm, A. 2013, in Astrophysics and Space Science Proceedings, Vol. 34, Cosmic Rays in Star-Forming Environments, ed. D. F. Torres & O. Reimer (Heidelberg: Springer), 331
Revnivtsev, M. G., Churazov, E. M., Sazonov, S. Yu., et al. 2004, A&A, 425, L49
Sadowski, A., Narayan, R., Penna, R., & Zhu, Y. 2013, MNRAS, 436, 3856
Schödel, R., Ott, T., Genzel, R., et al. 2002, Natur, 419, 694
Scoville, N. Z. 1972, ApJL, 175, L127
Snowden, S. L., Egger, R., Freyberg, M. J., et al. 1997, ApJ, 485, 125
Sofue, Y. 2000, ApJ, 540, 224
Spitzer, L. 1962, Physics of Fully Ionized Gases (2nd ed.; New York: Interscience)
Stone, J. M., & Norman, M. L. 1992, ApJS, 80, 753
Stone, J. M., & Pringle, J. E. 2001, MNRAS, 322, 461
Stone, J. M., Pringle, J. E., & Begelman, M. C. 1999, MNRAS, 310, 1002
Su, M., Slatyer, T. R., & Finkbeiner, D. P. 2010, ApJ, 724, 1044
Totani, T. 2006, PASJ, 58, 965
Vernaleo, J. C., & Reynolds, C. S. 2006, ApJ, 645, 83
Wang, Q. D. 2002, arXiv:astro-ph/0202317
Wang, Q. D., Nowak, M. A., Markoff, S. B., et al. 2013, Sci, 341, 981
Weaver, R., McCray, R., Castor, J., et al. 1977, ApJ, 218, 377
Xie, F., & Yuan, F. 2012, MNRAS, 427, 1580
Yang, H.-Y. K., Ruszkowski, M., Ricker, P. M., et al. 2012, ApJ, 761, 185
Yang, H.-Y. K., Ruszkowski, M., & Zweibel, E. 2013, MNRAS, 436, 2734
Yang, R., Aharonian, R., & Crocker, R. 2014, arXiv:1402.0403v1
Young, A. J., Wilson, A. S., & Mundell, C. G. 2002, ApJ, 579, 560
Yuan, F., Bu, D., & Wu, M. 2012a, ApJ, 761, 130
Yuan, F., & Narayan, R. 2004, ApJ, 612, 724
Yuan, F., & Narayan, R. 2014, ARA&A, in press (arXiv:1401.0586v1)
Yuan, F., Quataert, E., & Narayan, R. 2003, ApJ, 598, 301
Yuan, F., Wu, M., & Bu, D. 2012b, ApJ, 761, 129
Zubovas, K., & King, A. 2012, ApJL, 745, L34
Zubovas, K., King, A. R., & Nayakshin, S. 2011, MNRAS, 415, L21
Zubovas, K., & Nayakshin, S. 2012, MNRAS, 424, 666